

# Flight Test Results of an Adaptive Guidance System for Reusable Launch Vehicles

John D. Schierman,<sup>\*</sup> Jason R. Hull,<sup>†</sup> Neha Gandhi,<sup>‡</sup> and David G. Ward<sup>§</sup>

*BARRON ASSOCIATES, INC.*  
Charlottesville, VA 22901

## Abstract

For next generation Reusable Launch Vehicles (RLVs), reconfigurable control, adaptive guidance, and on-line trajectory-command reshaping will often be required to recover the mission in the face of a major anomalous event such as an effector failure. An adaptive guidance system that works in conjunction with a reconfigurable controller and an autonomous trajectory command reshaping algorithm is presented. The guidance law utilizes a backstepping architecture to generate pitch rate commands that drive the inner-loop control system. Under extreme failure conditions the control surfaces can saturate in an attempt to meet commanded moments. In these cases, the guidance feedback gains are reduced to preserve stability margins in the guidance loops.

In addition, simulation and flight test results of the complete reconfigurable control/adaptive guidance/trajectory reshaping system are presented for a simulated X-40A RLV. The Total In-Flight Simulator research aircraft was utilized to flight test the X-40A system under a variety of failure conditions. This work was completed in conjunction with the Air Force Research Laboratory's Integrated Adaptive Guidance & Control (IAG&C) program. Both simulation and flight test results indicate the major benefits of the new system. With on-line trajectory reshaping, the vehicle is able to achieve a safe touchdown, whereas the vehicle is lost without trajectory reshaping.

## I. Introduction

One of the overriding goals of recent NASA programs has been to develop new launch systems and space transportation architectures that are significantly safer, more reliable and less costly. Recent interest in access to space has seeded similar goals for the Air Force. Because of these interests, there is now significant concentration in reconfiguration technologies for the control and avionics systems of next generation *Reusable Launch Vehicles*, or *RLVs* [1], [2]. On-line reconfiguration can give the vehicle the capability to account for unexpected or unforeseen changes to the dynamics, aerodynamics, or control of the vehicle. Such changes may be due to, for example, control effector failures. However, RLVs typically do not possess the actuation redundancy or alternate control effectors seen in commercial or military aircraft, and this makes the reconfiguration task that much more challenging. Because of this, the reconfiguration problem will often involve not only the control of the vehicle, but also the guidance and the trajectory command functions as well.

A unique approach to the RLV on-line reconfiguration/adaptation problem is discussed herein. Along with a reconfigurable control system, this approach involves two main elements:

---

<sup>\*</sup> Senior Research Scientist, 1410 Sachem Pl., Ste. 202, Associate Fellow, AIAA.

<sup>†</sup> Research Scientist, 1410 Sachem Pl., Ste. 202.

<sup>‡</sup> Research Associate, 1410 Sachem Pl., Ste. 202.

<sup>§</sup> Senior Research Scientist, 1410 Sachem Pl., Ste. 202, Senior Member, AIAA.

1. *Guidance gain adaptation:* An adaptive backstepping approach [3] has been developed to deliver commands to the inner-loop control system. Following an effector failure, information regarding control saturation and/or inner-loop bandwidth reduction is identified on-line and delivered to algorithms that adapt the feedback gains of the guidance law. Flight path stability is then maintained in the face of degraded maneuvering capabilities.
2. *On-line trajectory command reshaping:* Even with flight path stability maintained, the trajectory commands driving the guidance system may need to be continually reshaped on-line in order to achieve desired end conditions of the mission segment (e.g. on final approach, desired end conditions are characterized by a soft landing, at a certain runway touchdown point, at a certain flight speed). The approach discussed here is denoted as the *Optimum-Path-To-Go (OPTG)* algorithm [4], [5], [6] [7]. Polynomial networks describing the “best” remaining path to the end of the mission segment are interrogated on-line at regular intervals to obtain the optimal trajectory commands, given the current state and “health” of the vehicle.

The work presented herein was jointly funded by both the Air Force Research Lab (AFRL) and NASA, Marshall Space Flight Center (MSFC). A detailed design of the adaptive guidance system and on-line trajectory command-reshaping algorithm was integrated with a reconfigurable control system designed by AFRL [8]. The demonstration platform for this development was Boeing’s X-40A RLV, shown in Figure 1. This is an unpowered test bed vehicle with autonomous control and guidance. The X-40A is a technology demonstrator for its orbital counterpart, the X-37. The control effectors modeled for the X-40A are:



**Figure 1. Boeing’s X-40A RLV in Drop Tests.**

1. Left and right ruddervators: much like missile fin surfaces, these act as both pitch (asymmetric deflection) and yaw/roll (symmetric deflection) control effectors.
2. Left and right flaperons: these act as both lift generating devices (symmetric deflection) and as ailerons for roll control (asymmetric deflection).
3. Speedbrake: this is a surface on the top of the fuselage between the ruddervators, and can be deflected upward to 70 deg. It is nominally deflected to approximately 20 deg. so that the velocity can be controlled in both directions (reduce deflection to speed up, increase deflection to slow down). Under certain failure scenarios, the speedbrake can be employed to produce some pitching moment.
4. Bodyflap: this surface is hinged at the aft of the fuselage, similar in configuration to the Space Shuttle’s body flap. Under nominal operations, this surface is used for pitch trim control, but may be used for active pitch control under failures.

Note that although the X-40A is modeled here to include a speedbrake and bodyflap, the actual vehicle is not equipped with these devices. However, the X-37 RLV is equipped with these effectors. The actuator models and the influence of these effectors on the X-40A vehicle dynamics were drawn from the X-37 simulation model. These additional control effectors were included in the demonstration vehicle to allow for more varied failure and reconfiguration studies, and to facilitate transition to the X-37 program.

The algorithms developed in this effort were then successfully flight tested under the AFRL-funded Integrated Adaptive Guidance & Control (IAG&C) program [7]. The flight tests were completed by the Flight and Aerospace Research Group, General Dynamics Advanced Information Systems (GDAIS) - formally Veridian – using the Total In-Flight Simulator (TIFS) research aircraft, shown in Figure 2. The TIFS simulated autonomous approach/landings



**Figure 2. GDAIS's Total In-Flight Simulator (TIFS) Research Aircraft.**

of the X-40A under a variety of single and multiple control surface failure experiments. The majority of the flight test results indicated the significant benefits of the control reconfiguration, guidance adaptation and trajectory-command reshaping, concluding in successful touchdown conditions. Although most touchdowns were simulated at an altitude of 200 feet, the safety pilots of the TIFS vehicle were comfortable enough with the simulated (unpiloted) system to allow some of the experiments to complete actual touchdowns.

The OPTG trajectory command-reshaping algorithm and reconfigurable control system have been presented in detail in [4] through [8]. Details of the adaptive guidance system will be presented next, followed by a brief summary of the OPTG algorithm. Simulation and flight test results will then be presented that show the benefits of the integrated reconfigurable control, adaptive guidance, and trajectory command reshaping system.

## II. Design Overview

An overview of the design architecture is given in Figure 3. Again, the inner-loop reconfigurable controller was developed by AFRL. The final design of this controller involved a perfect model-following approach with optimal control allocation to enable control reconfiguration. Further details of this design can be found in [7] and [8]. The adaptive backstepping guidance law delivers a pitch rate command to the inner-loop control law. Boeing's lateral guidance law was adopted to deliver yaw rate and roll rate commands. The lateral guidance law will not be covered in this paper, as the majority of failure cases experienced little lateral-directional motion, and the main focus of the flight test experiments was on the longitudinal guidance problem.

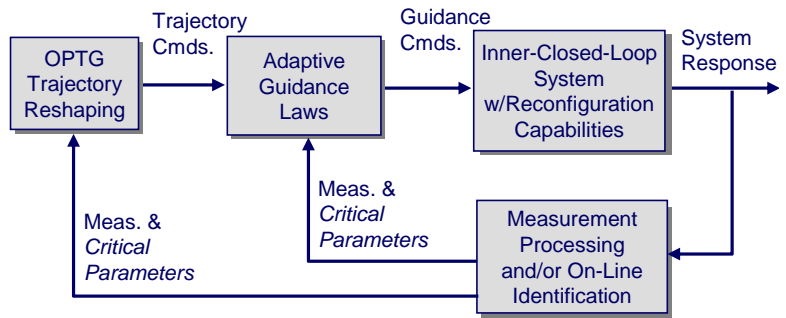


**Figure 3. Overview of Design Architecture.**

As indicated in Figure 3, both measurements and critical parameters are supplied to the OPTG trajectory reshaping algorithm and the adaptive guidance laws. Following an anomalous event such as a control effector failure, critical parameters are those measurable (or reconstructable) quantities that convey the key aspects of the vehicle's performance degradations to the outer-loop guidance reconfiguration or trajectory reshaping functions. For the current study, the critical parameter for guidance law adaptation is the inner-loop controller's reference model bandwidth (a design parameter) which is used to schedule outer-loop guidance gains. The critical parameters for trajectory reshaping are upper and lower bounds on achievable lift and drag forces, identified on-line. Analogous to the "attainable moment set," often discussed in inner-loop attitude control studies, the lift and drag bounds parameterize all possible failures and anomalous conditions that affect the vehicle's ability to generate these forces. For example, the commanded trajectory may be reshaped in the same fashion for an unforeseen headwind as it would for a particular locked control surface that would add approximately the same amount of additional axial force. The lift and drag bound estimates are fed to the OPTG trajectory-reshaping algorithm to determine the appropriate trajectory to follow. The OPTG algorithm then delivers altitude and flight path angle commands to the longitudinal guidance law.

### III. X-40A Adaptive Guidance Law Design.

#### A. Design Overview

Backstepping is a control approach by which “pseudo commands” are generated at each loop closure that drives the next-most inner loop. These commands are derived by dynamic inversion. Consider plant dynamics expressed as,

$$\dot{x} = f(x) + g(u) \quad (1)$$

The objective of dynamic inversion is to generate a control law that “cancels” the plant dynamics and follows a desired state rate,  $\dot{x}_{des}$ . Dynamic inversion takes on various forms depending on how  $\dot{x}_{des}$  is generated, and how plant-modeling errors are dealt with. A fundamental form for a dynamic inversion control law is:

$$u^* = g^{-1}\{\dot{x}_{des} - f(x)\} \quad (2)$$

where  $g^{-1}$  is defined such that  $g(g^{-1}(u)) = u$ .

For fixed-wing aircraft systems such as the X-40A, a natural loop-closure architecture for longitudinal guidance is:

- i. Altitude loop (outer most loop) to
- ii. Flight-path-angle loop to
- iii. Angle-of-attack loop (inner-most loop).

The last loop then generates the pitch rate command,  $Q_c$ , that drives the inner-closed-loop pitch dynamics. This architecture is depicted in Figure 4. Note that the trajectory reshaping algorithm delivers altitude, flight path angle, and flight path angle rate commands ( $H_c, \gamma_c, \dot{\gamma}_c$ ) to the guidance law. These parameters define the commanded trajectory. Also, see that the reference model pitch-loop bandwidth,  $K_{bw_Q}$ , is fed back to each block for gain adaptation purposes. The guidance laws depicted in each block in Figure 4 will be discussed in more detail below.

Again, Boeing’s original lateral guidance law was adopted to deliver roll and yaw rate commands to the inner-loop control law. The approach/landing flight condition consists largely of vertical plane motion; therefore, lateral adaptive guidance and lateral trajectory reshaping designs were not pursued in this program.

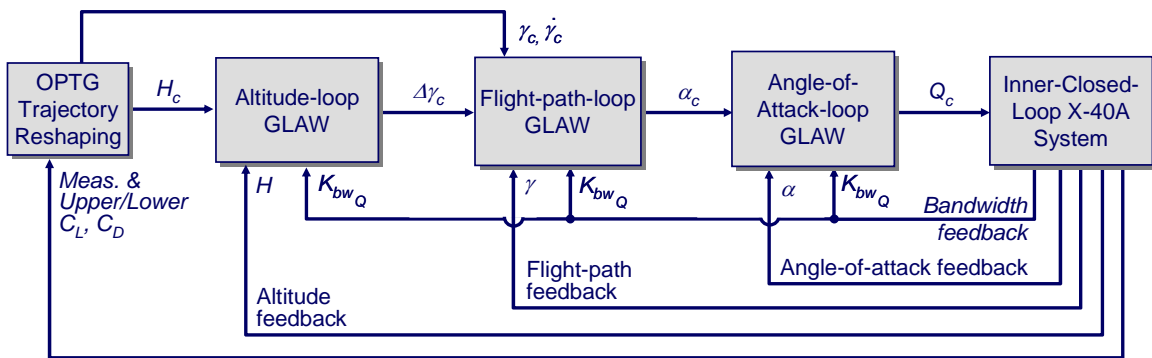


Figure 4. Backstepping Guidance Law Architecture.

#### B. Altitude Loop Guidance Law

Using the design paradigm just described, we start with the altitude loop to formulate the appropriate flight-path-angle command. The governing equation of motion here is:

$$\dot{H} = V \sin(\gamma) \quad (3)$$

where  $H$  = altitude,  $V$  = airspeed, and  $\gamma$  = flight path angle. Defining,

$$\begin{aligned} f_H(H) &\triangleq 0 \\ g_H(\gamma) &\triangleq V \sin(\gamma) \Rightarrow g_H^{-1}(\cdot) = \sin^{-1}\left(\frac{\cdot}{V}\right) \end{aligned} \quad (4)$$

Then Eq. (3) may be expressed as

$$\dot{H} = f_H(H) + g_H(\gamma) \quad (5)$$

Therefore, as in Eq. (2), solving for  $\gamma$ , the flight-path-angle command can be derived as:

$$\gamma_c = g_H^{-1}(\dot{H}_{des} - f_H(H)) \quad (6)$$

Substitution of Eq. (4) into Eq. (6) gives

$$\gamma_c = \sin^{-1}(\dot{H}_{des}/V) \quad (7)$$

Note from Figure 4 that the altitude loop backstepping guidance law delivers a corrective flight-path angle command, or  $\Delta\gamma_c$ . Therefore,

$$\Delta\gamma_c = \sin^{-1}(\Delta\dot{H}_{des}/V) \triangleq Z_\gamma^{-1} \quad (8)$$

The corrective sink rate command,  $\Delta\dot{H}_{des}$ , is derived from PI control on altitude error. In the Laplace domain,\*\* this can be expressed as,

$$\Delta\dot{H}_{des}(s) = \left( K_H + \frac{K_{H_i}}{s} \right) (H_c(s) - H(s)) \quad (9)$$

where the altitude command,  $H_c(s)$  is derived from the OPTG algorithm. From the above equations, the altitude loop backstepping guidance law is depicted in Figure 5, where  $Z_\gamma^{-1}$  is defined in Eq. (8). Note that the dependence on the reference model pitch-loop bandwidth,  $K_{bw_Q}$ , is not yet indicated. Also not yet indicated is that the feedback gain,  $K_H$ , is adaptive. These topics are discussed later.

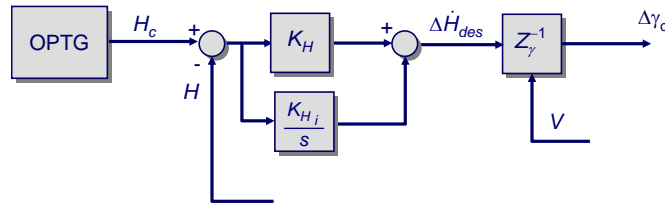


**Figure 5. Altitude Loop Backstepping Guidance Law.**

\*\* PI control is presented here in the familiar Laplace domain (i.e. for continuous systems) for clarity. However, the actual implementation of all the algorithms was in the discrete-time domain.

### C. Flight Path Loop Guidance Law

Next, we turn attention to the flight-path-angle loop to formulate the appropriate angle-of-attack command. The governing equation of motion here is:

$$\dot{\gamma} = \frac{L}{mV} - \frac{g}{V} \cos(\gamma) \quad (10)$$

where  $m$  = vehicle mass and  $g$  = gravitational acceleration. It is assumed here that total vehicle lift,  $L$ , can be expressed as follows:

$$L = L_o + L_\alpha \alpha + \{L_\delta\} \vec{\delta} \quad (11)$$

where  $\alpha$  = angle-of-attack,  $L_o$  is lift at zero angle-of-attack,  $L_\alpha$  is the dimensional lift-curve slope,  $\{L_\delta\}$  is a row vector of lift increment due to each control surface deflection, and  $\vec{\delta}$  is the vector of control surface deflection values. Defining

$$L' = L_o + \{L_\delta\} \vec{\delta} \quad (12)$$

then,

$$L = L' + L_\alpha \alpha \quad (13)$$

Substituting Eq. (13) into Eq. (10) gives:

$$\dot{\gamma} = -\frac{g}{V} \cos(\gamma) + \frac{L'}{mV} + \frac{L_\alpha}{mV} \alpha \quad (14)$$

Defining,

$$\begin{aligned} f_\gamma(\gamma) &\triangleq -\frac{g}{V} \cos(\gamma) + \frac{L'}{mV} \\ g_\gamma(\alpha) &\triangleq g_\gamma \alpha = \frac{L_\alpha}{mV} \alpha \Rightarrow g_\gamma^{-1} = \frac{mV}{L_\alpha} \end{aligned} \quad (15)$$

Then Eq. (14) may be expressed as

$$\dot{\gamma} = f_\gamma(\gamma) + g_\gamma \alpha \quad (16)$$

Therefore, as in Eq. (2), solving for  $\alpha$ , the angle-of-attack command can be derived as:

$$\alpha_c = g_\gamma^{-1} (\dot{\gamma}_{des} - f_\gamma(\gamma)) \quad (17)$$

Substitution of Eq. (15) into Eq. (17) gives

$$\alpha_c = \frac{mV}{L_\alpha} \left( \dot{\gamma}_{des} + \frac{g}{V} \cos(\gamma) - \frac{L'}{mV} \right) \triangleq Z_\alpha^{-1} \quad (18)$$

PI control is again used to derive the desired flight path angle dynamics. Therefore, the desired flight path angle rate is defined in the Laplace domain as:

$$\dot{\gamma}_{des}(s) = \dot{\gamma}_c(s) + \left( K_\gamma + \frac{K_{\gamma_i}}{s} \right) (\gamma_c(s) + \Delta\gamma_c(s) - \gamma(s)) \quad (19)$$

where the flight path angle and flight path angle rate commands,  $\gamma_c(s)$ ,  $\dot{\gamma}_c(s)$ , are derived from the OPTG algorithm. Again, the corrective term on the flight path angle command,  $\Delta\gamma_c(s)$ , is derived from the altitude loop guidance law (see Eq. (8)). From the above equations, the flight-path loop backstepping guidance law is depicted in Figure 6 below, where  $Z_\alpha^{-1}$  is defined in Eq. (18). Here too, the dependence on the reference model pitch-loop bandwidth,  $K_{bw_Q}$ , is not yet indicated, and that the feedback gain  $K_\gamma$  is adaptive is also not yet indicated.

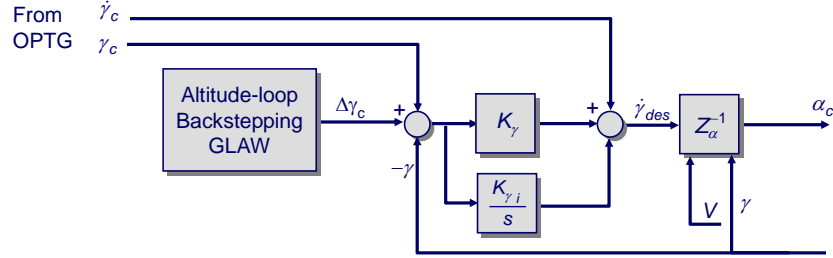


**Figure 6. Flight-Path Loop Backstepping Guidance Law.**

#### D. Integrator Anti-Windup Logic

Integrator anti-windup logic was added to help preserve stability when saturation occurs in either the angle-of-attack loop or pitch-axis saturation occurs in the inner loop control allocator. The angle-of-attack command is limited between  $-5$  and  $24$  degrees (the bounds of the aerodynamic database). If the angle-of-attack command needs to exceed this limit in order to track the trajectory, the integrator states will quickly grow due to tracking errors. A similar situation will occur if the inner loop becomes saturated and can no longer achieve the pitch rate command. When either of these situations arises, the integrator states in the altitude and flight-path loops are held at their current values.

#### E. Angle-of-Attack Loop Guidance Law

Lastly, attention is turned to the angle-of-attack loop to formulate the appropriate pitch rate ( $Q$ ) command for the inner-loop control law. From pitch attitude,  $\theta = \alpha + \gamma$ , and ignoring lateral-directional influences on the pitch rate so that  $Q = \dot{\theta}$ , the governing equation of motion here is:

$$\dot{\alpha} = -\dot{\gamma} + Q \quad (20)$$

or,

$$\dot{\alpha} = \frac{g}{V} \cos(\gamma) - \frac{L'}{mV} - \frac{L_\alpha}{mV} \alpha + Q \quad (21)$$

Defining,

$$f_\alpha(\gamma, \alpha) \triangleq \frac{g}{V} \cos(\gamma) - \frac{L'}{mV} - \frac{L_\alpha}{mV} \alpha \quad (22)$$

$$g_\alpha(Q) \triangleq Q \Rightarrow g_\alpha^{-1} = 1$$

Then Eq. (21) may be expressed as

$$\dot{\alpha} = f_\alpha(\gamma, \alpha) + g_\alpha Q \quad (23)$$

Therefore, as in Eq. (2), solving for  $Q$ , the pitch rate command can be derived as:

$$Q_c = g_\alpha^{-1}(\dot{\alpha}_{des} - f_\alpha(\gamma, \alpha)) \quad (24)$$

Substitution of Eq. (22) into Eq. (24) gives

$$Q_c = \dot{\alpha}_{des} - \frac{g}{V} \cos(\gamma) + \frac{L'}{mV} + \frac{L_\alpha}{mV} \alpha \triangleq Z_Q^{-1} \quad (25)$$

We seek stable, first order angle-of-attack tracking. Hence, the desired angle-of-attack dynamics are defined as:

$$\dot{\alpha}_{des} = K_\alpha (\alpha_c - \alpha) \quad (26)$$

where  $\alpha_c$  is the angle-of-attack command generated from the flight-path loop backstepping guidance law (Eq. (18)). From the above equations, the angle-of-attack loop backstepping guidance law is depicted in Figure 7, where  $Z_Q^{-1}$  is defined in Eq. (25).

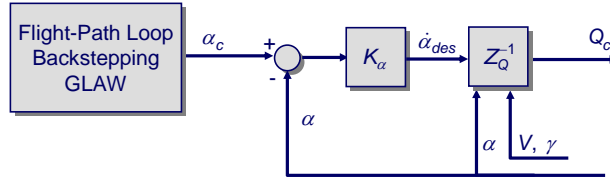


**Figure 7. Angle-of-Attack Loop Backstepping Guidance Law.**

#### F. Guidance Law Gain Adaptation

The proportional gains within each block of the guidance law are adapted based on the control system’s reference model pitch-loop bandwidth,  $K_{bw_Q}$ , (which, recall, is reduced when the inner-loop pitch axis becomes saturated). In particular, the proportional gains are designed to be linear functions of the pitch axis bandwidth, and this relationship was designed via “loop shaping” considerations. In this manner, when the pitch axis bandwidth is reduced, the proportional gains in each of the guidance loops are reduced to maintain stability robustness margins. The adaptation laws used for the flight test program are given in Table 1. It should be noted that non-adaptive systems often contain logic to address control saturation. The approach here is deemed “adaptive” because the feedback gains adapt to changes in the inner-loop bandwidth. Although here such changes are due to saturation, the approach can be generalized to address other reasons for bandwidth changes. For example, in some vehicles, not all actuators have equivalent bandwidth capabilities, and if high-bandwidth, primary control effectors fail, slower actuators may have to be utilized in the inner-loop control reconfiguration. In such a case, there will be an overall reduction in inner-loop bandwidth - not due to saturation. The adaptive guidance scheme presented here would be able to address that class of control failures.

**Table 1. Guidance Loop Gain Adaptation Law.**

	<i>Factor of Inner Loop Bandwidth</i>	<i>Nominal Gain Value</i>
Altitude Loop, $K_H$	1/15	0.2
Gamma Loop, $K_\gamma$	1/5	0.6
Alpha Loop, $K_\alpha$	5/9	1.67

It was found that the guidance loop gain adaptation was not typically necessary for the case studies involved with the flight tests (although high wind gust conditions were seen to cause axis saturation and subsequent guidance adaptation). Therefore, this element of the overall system was not rigorously tested. Further testing of this adaptation approach may yield more maturation of the design approach, including adaptation of the integrator gains. The integrator gains were not adapted with this scheme since their adaptation was addressed via the anti-windup

logic described in Subsection D. The overall guidance law architecture, including the gain adaptation is depicted in the block-diagram presented in Figure 8.

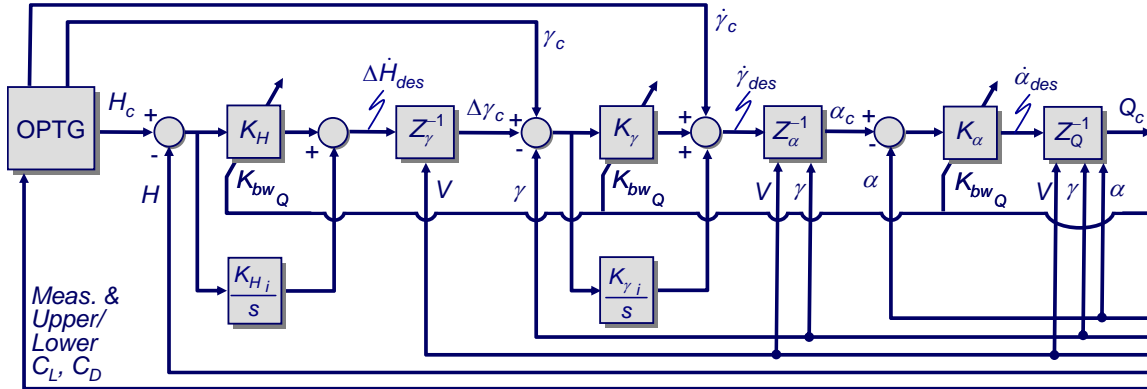


Figure 8. Backstepping Guidance Law Architecture with Adaptive Feedback Gains.

### G. Final Flare Guidance Law

Near touchdown, the primary objective is to arrest the sink rate in preparation for landing. This is accomplished in the final flare guidance law. At an altitude of 150 feet, the backstepping guidance law is turned off, and the final flare guidance law is enabled (or Pmode\_4 in Shuttle-heritage guidance law terminology). In this mode, an exponential altitude profile is tracked instead of tracking the trajectory provided by the OPTG algorithm. This profile is generated using a linear relationship between altitude and sink rate, as shown in Figure 9. That is,

$$\dot{H}_c = -\frac{H}{\tau_{ff}} + \dot{H}_{des} \quad (27)$$

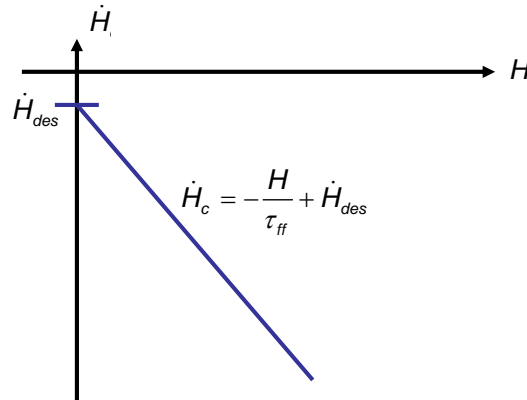


Figure 9. Altitude -vs- Sink Rate Profile During Final Flare Guidance.

By adjusting the time constant  $\tau_{ff}$  the exponential profile can be made more or less aggressive. The time constant is chosen automatically at the start of the final flare to preserve continuity in the sink rate profile. That is,

$$\tau_{ff} = (150 \text{ ft}) / (\dot{H}_{des} - \dot{H}_{@150 \text{ ft}}) \quad (28)$$

In addition to preserving continuity, this scheme selects a more or less aggressive time constant depending on the magnitude of the sink rate at 150 ft. Lastly, it was defined that  $\dot{H}_{des} = -2 \text{ fps}$ .

The sink rate command is converted into a flight path angle command using the same relationship as before,  $\gamma_c = \sin^{-1}(\dot{H}_c/V)$  (see Eq. (7)). Note, however, there is no longer a corrective term on the flight path angle command (from the altitude loop guidance law) because, again, the primary objective of the final flare guidance is to arrest the sink rate to achieve a soft landing. Therefore, following flight path angle is less important than tracking the desired sink rate profile. This scheme has been found to be robust to disturbances and other variations, consistently achieving touchdown sink rates well within the acceptable limit (around -9 to -10 fps).

#### IV. X-40A Trajectory Command Reshaping Design – Summary

The OPTG trajectory-reshaping algorithm is tasked to find a re-targeted trajectory that requires only forces and moments that can be achieved by the degraded capabilities of the vehicle while meeting certain critical constraints. As shown in Figure 4, the re-targeted trajectory is expressed in terms of altitude, flight path angle and flight path angle rate commands. These commands, derived from the on-line OPTG algorithm, drive the guidance loops. The main steps to the OPTG design protocol are listed below.

##### A. OPTG Protocol

1. Off-Line Trajectory Optimization Formulation: For the mission segment under study, a trajectory optimization problem is first formulated by defining the objective function, boundaries of admissible initial/final conditions, admissible variations in critical parameters (again, bounds on trim lift and drag), any particular constraints and the appropriate governing equations of motion. Once properly formulated, candidate trajectories can be readily obtained.
2. Off-Line Trajectory Database Generation: A database of neighboring extremals is generated by successively varying initial conditions and critical parameters. Such trajectories represent optimal flight paths for the vehicle under failure conditions. Libraries of trajectory databases are generated by repeating this procedure for several downrange locations (usually in equally spaced intervals). This large volume of trajectory data can be cumbersome to interrogate on-line with traditional table lookup methods. The next step in the OPTG approach solves this problem.
3. Off-Line Trajectory Encoding: This aspect of the OPTG methodology is the most important in terms of enabling on-line use. First, from the set of neighboring extremals found in Step 1, the states of the systems are modeled as a set of selected basis functions most appropriate for the mission segment. Polynomials in downrange have been selected here for the approach-to-landing flight phase, which is largely 2-dimensional flight (vertical plane motion). A nonlinear function-modeling tool is then used to generate polynomial neural networks (PNNs) that map the current vehicle observables (states and critical parameters) to the coefficients of the basis functions describing the associated trajectory. These mappings relate the observables to the basis function coefficients in an efficient, compact manner.
4. On-Line PNN Interrogation: The final step in the OPTG approach is performed on-line. During flight, the current vehicle states and critical parameters are obtained from measurements or reconstructed from an on-line identification algorithm. This information is then used to compute an appropriate set of basis function coefficients by interrogating the PNNs. Sensor noise and atmospheric disturbances, such as gusts or unpredicted winds, are difficult to include in a trajectory database and thus would not be represented in the PNN models. To be robust to such disturbances and errors, the PNNs are augmented with an on-line coefficient correction algorithm to ensure that the final conditions are met (here, a simple least-squares fit routine has been seen to work quite well). The trajectory commands are then calculated from the corrected basis functions. The loop is closed by re-interrogating the PNNs at regular intervals – typically on the order of 1 Hz. In this manner, trajectories are reshaped in flight to account for changes in the vehicle dynamics due to control surface failures or other significant anomalous events.

As stated, the details of the OPTG design can be found in [6] as well as [7]. However, for completeness, a review of the trajectory optimization formulation is given below.

## B. Trajectory Optimization Formulation

System states appropriate for the approach/landing flight phase are:

$$\begin{aligned} V &= \text{velocity} \\ \gamma &= \text{flight path angle} \\ X &= \text{downrange} \\ H &= \text{altitude} \end{aligned}$$

with the corresponding governing equations of motion:

$$\begin{aligned} \dot{V} &= \frac{-D}{m} - g \sin(\gamma), \quad D = \bar{q} S C_D(\alpha, M) \\ \dot{\gamma} &= \frac{L}{mV} - \frac{g}{V} \cos(\gamma), \quad L = \bar{q} S C_L(\alpha, M) \\ \dot{X} &= V \cos(\gamma) \\ \dot{H} &= V \sin(\gamma) \end{aligned} \quad (29)$$

Here,  $D$  = Drag,  $L$  = Lift,  $g$  = acceleration of gravity,  $m$  = vehicle mass,  $\bar{q}$  = dynamic pressure,  $S$  = wing area,  $C_D$  and  $C_L$  are the drag and lift coefficients, respectively,  $\alpha$  = angle of attack, and  $M$  = Mach no. To attain additional robustness, common practice in RLV trajectory optimization is to change the independent variable from time to a monotonic parameter. An appropriate choice for approach/landing guidance is downrange position,  $X$ . To do this, each state equation is multiplied by

$$\frac{dt}{dX} = \frac{1}{V \cos(\gamma)} \quad (30)$$

resulting in:

$$\begin{aligned} \frac{dV}{dX} &= \dot{V} \frac{dt}{dX} = V_X = \frac{-D}{mV \cos(\gamma)} - \frac{g}{V} \tan(\gamma) \\ \frac{d\gamma}{dX} &= \dot{\gamma} \frac{dt}{dX} = \gamma_X = \frac{L}{mV^2 \cos(\gamma)} - \frac{g}{V^2} \\ \frac{dH}{dX} &= \dot{H} \frac{dt}{dX} = H_X = \tan(\gamma) \end{aligned} \quad (31)$$

Eq. (30) can be eliminated from consideration since the governing equations are time-invariant and there are no boundary conditions on time (it is not of concern how long it takes for the RLV to arrive at touchdown). Hence, an added benefit of the new parameterization is that it reduces the dimensionality of the search domain in the optimization problem.

The optimization problem is formulated as a Successive Quadratic Programming (SQP) [9] problem. For the SQP method, the states and command or decision variables are partitioned into  $N$  discrete points. It was found that  $N = 100$  is an appropriate choice for approach/landing trajectories. At each point, an approximation is made that generates a solvable quadratic programming *sub-problem* whose solution is used to form the search direction.

The optimization problem is formalized as follows:

$$\begin{aligned} \min_{\substack{C_L \in \mathbb{R}^N \\ X_f \in \mathbb{R}}} J &= (\dot{H}^T W \dot{H})^{1/2}, \quad \dot{H} = f(C_L, X_f) \end{aligned} \quad (32)$$

The objective of the cost function is to minimize vertical acceleration,  $\ddot{H}$ , which is related to the vehicle's normal acceleration,  $N_z$ . This allows for smoother, less aggressive trajectories, especially beneficial under control failure scenarios. The weighting matrix,  $W$ , is defined as:

$$W = \text{diag}[1 \quad 1 + \frac{1}{N-1} \quad 1 + \frac{2}{N-1} \cdots \quad 2] \quad (33)$$

This weighting scheme emphasizes minimizing accelerations at the end of the trajectory, resulting in less aggressive flares.

The downrange touchdown position,  $X_f$ , has an overriding influence on the shape of the trajectories. Therefore, this is included as a decision variable. As expected, for low-energy scenarios, the optimal touchdown point is often near the beginning of the runway, and for high-energy scenarios, it is typically farther down the runway. The other decision variable is the lift coefficient history, defined as

$$C_L = [C_{L_1}, C_{L_2}, \dots, C_{L_k}, \dots, C_{L_N}]^T \quad (34)$$

Both the lift and drag coefficients are constrained to be within their respective upper and lower bounds, as

$$\begin{aligned} C_{L_{min}} &\leq C_{L_i} \leq C_{L_{max}}, \quad i = 1, \dots, N \\ C_{D_{min}} &\leq C_{D_i} \leq C_{D_{max}}, \quad i = 1, \dots, N \end{aligned} \quad (35)$$

The lift coefficient is considered the single forcing input to the governing equations of motion, as it is assumed that the drag is a linear function of lift. That is, it is modeled that

$$C_{D_i} = \left( \frac{C_{D_{max}} - C_{D_{min}}}{C_{L_{max}} - C_{L_{min}}} \right) C_{L_i} + \frac{C_{D_{min}} C_{L_{max}} - C_{D_{max}} C_{L_{min}}}{C_{L_{max}} - C_{L_{min}}}, \quad i = 1, \dots, N \quad (36)$$

Typically, drag is more of a parabolic function of lift; however, at this stage it is convenient to describe the lift and drag characteristics by two points, their maximum and minimum (i.e.  $\{C_{L_{min}}, C_{D_{min}}\}$ ,  $\{C_{L_{max}}, C_{D_{max}}\}$ ). Further, this linear approximation was not found to be limiting because the lift and drag coefficients are determined from a trimmed solution, which is not unique.<sup>††</sup> That is, in reality, the lift-drag relationship is characterized by a range of parabolas, and the linear relationship used here lies within this range.

Lastly, the optimization is subject to the following terminal constraints:

$$\begin{aligned} X_{f_{min}} &\leq X_f \leq X_{f_{max}} \\ V_f &\leq V_{f_{max}} \\ \dot{H}_f &\geq \dot{H}_{f_{min}} \\ H_f &= H_{Rnwy} \end{aligned} \quad (37)$$

The downrange touchdown position is constrained to be between the end of the runway and the point at which the minimum distance required to stop is reached (with margin included). This is defined to be:  $0 \text{ ft} \leq X \leq 10,000 \text{ ft}$ . (this large range is appropriate for the vehicle under study, as RLVs will typically be targeted to exceptionally long runways or dry lake beds for risk mitigation). For the final velocity,  $V_{f_{max}} = 300 \text{ fps}$ . Much beyond this value and

---

<sup>††</sup> The particular trimmed solution used here minimized control surface deflections from zero deg. deflection for all surfaces except speedbrake, which was nominally deflected to 20 deg.

tire blowout can occur. For touchdown sink rate,  $\dot{H}_{f_{min}} = -10 \text{ fps}$ . Damage to the vehicle can occur for sink rates harder than this limit. Lastly, the final altitude is set to the runway altitude,  $H_{Rmwy}$ .

Note that, within the SQP algorithm, the terminal values are found by numerically integrating the system in Eq. (31) from an initial downrange,  $X_o$ , to the final touchdown point,  $X_f$ , driven by the  $N$  decision variables in the “command vector”  $C_L$ . In this manner, the state equations are implicitly satisfied even though they are not directly defined as constraints.

## V. High Fidelity Simulation Results

Flight of the X-40A during approach/landing was studied under both nominal conditions (all control surfaces working) and for a significant number of *locked* control surface failure cases. Due to programmatic constraints, the focus of failure experiments was limited to locked surfaces, as this was deemed one of the more probable types of failures. Other classes of failures, such as floating, missing, damaged, or partially working surfaces would have to be investigated in further developments of this approach.

### A. Batch Simulation Results

The final phase of batch simulation experiments was conducted just prior to the final phase of flight tests, and these results are presented in Table 2. These results were obtained from the high fidelity 6-dof simulation model for the X-40A, developed for the IAG&C flight test program. This simulation includes high fidelity aerodynamic and actuator models, and geodetic, navigation and measurement processing modules provided by Boeing. These elements are integrated with the final control, guidance and trajectory reshaping designs. At this late stage in the design cycle, study focused on severe failure cases in which two or more control effectors were locked in place. These represent good candidates for scenarios requiring in-flight trajectory reshaping, having significant effect on lift and drag limits. In the table, BF = bodyflap, Rud = ruddervator, Flap = flaperon, and SB = speedbrake. For all cases presented in Table 2 both the control reconfiguration and guidance gain adaptation functions are enabled. Without at least these capabilities, the vehicle will fail to achieve a safe landing. Each failure class listed in the table represents a number of specific failures studied, where the control surfaces that were failed were locked in position at certain intervals throughout their deflection ranges. For example, the bodyflap is failed in increments of 5 deg. from its full deflection down to its full deflection up. Deflection of the ruddervators is more sensitive, and these are failed in increments of 1 deg. from  $\pm 3$  deg. limits. Similar failure suites are defined for the other control surfaces. A total of 2,518 cases were run in this experiment, representing various combinations of failed surfaces and deflections at which the surfaces were locked. Table 2 presents results for the IAG&C system with and without the OPTG trajectory reshaping enabled. Listed are the percent of successful touchdowns, where success is defined by the touchdown criteria listed in Table 3.

The results indicate that the IAG&C system is fairly robust to a wide array of multiple surface failures even without trajectory reshaping. Approximately 59% of the cases result in successful touchdown conditions for the vehicle tracking the nominal commanded trajectory. The majority of these cases are recovered due to the inner-loop control reconfiguration alone. However, a substantial improvement is seen when trajectory reshaping is enabled. Under these cases, approximately 95% of the runs result in successful touchdowns. The 5% of un-recovered cases are failures so severe that loss of the vehicle occurs even with trajectory reshaping. These cases usually involve either a flaperon failure or double ruddervator failures in combination with another locked control surface. All remaining control power is allocated to simply maintain vehicle stability, leaving little to no margin for maneuvering the vehicle, especially through the main flare. Under these cases, the vehicle will fly straight into the ground, far short of the runway.

**Table 2. Summary of Failure Classes Investigated.**

<i>Class of Failure</i>	<i>Number of Cases</i>	<i>% Success w/o Reshaping</i>	<i>% Success w/Reshaping</i>
BF + Rud (Both)	89	42	77
BF + Flap (Left)	21	57	100
BF + SB	1599	60	100
SB + Rud (Both)	639	63	89
SB + Flap (Left)	81	21	76
Flap (Left) + Rud (Both)	89	82	94
<b>Total</b>	<b>2518</b>	<b>59</b>	<b>95</b>

**Table 3. Touchdown Specifications.**

<i>Touchdown Specification</i>	<i>Failure to meet specs.</i>
Sink rate $\geq -10$ fps.	Landing gear or structural damage
Pitch angle $\leq 15$ deg.	Tail scrape
Groundspeed $\leq 310$ fps.	Tire blowout
Downrange $\leq 10,000$ ft.	Wheel stop off runway

**B. Sample Case Study**

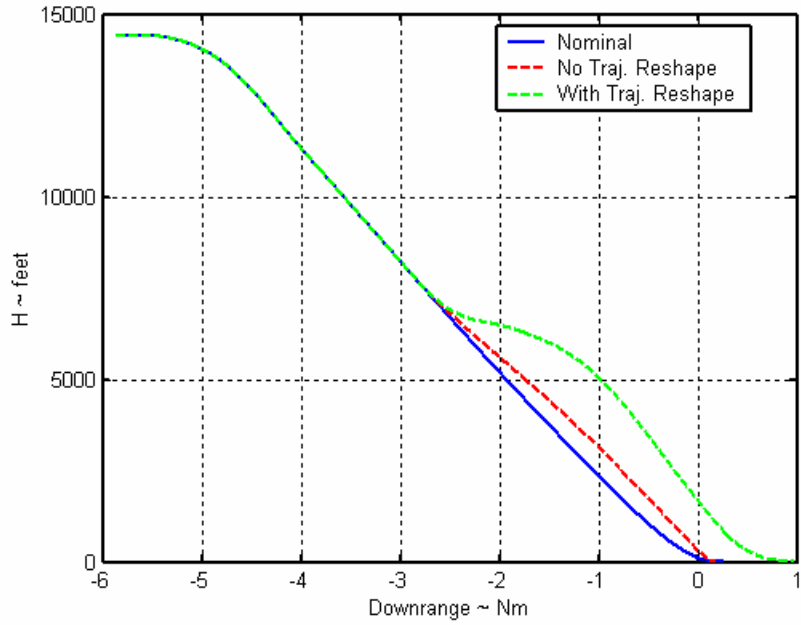
In this section we present an extreme failure case that still resulted in a successful recovery in high-fidelity simulation. These results are typical for a significant number of the extreme failure cases studied that involved different control surfaces or combinations of control surfaces at various failure deflection values. The failure was defined as:

Body flap failed at -3 deg. (trailing edge up)  
Both left and right ruddervators failed at 0 deg.

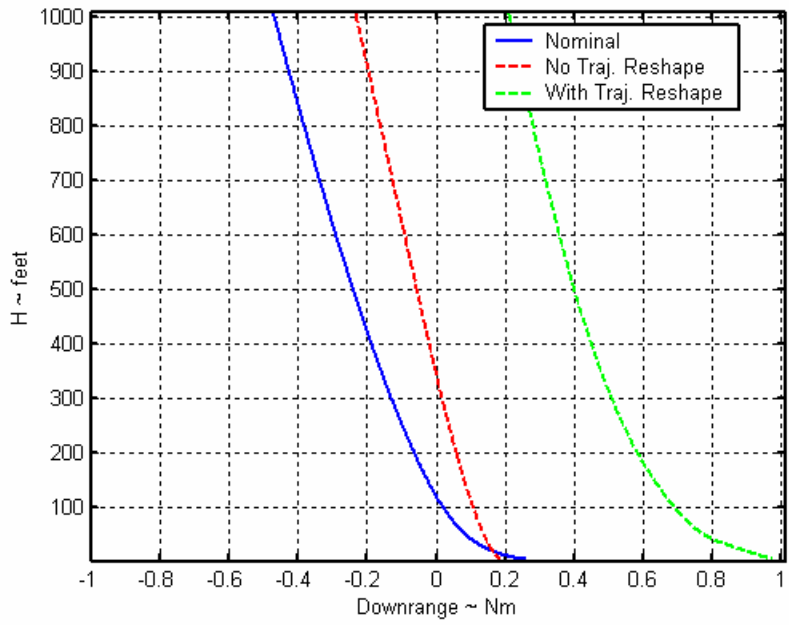
In this case, three of the six available control surfaces have failed. The failure occurs at approximately 2.5 nautical miles down range.

Figure 10 presents the trajectory profile (altitude –vs- downrange). Plotted are the nominal (no failure) trajectory in the blue solid line, the trajectory for the vehicle with no on-line trajectory reshaping in the red dashed line, and the trajectory for the vehicle with on-line reshaping in the green dashed line. Note that for both cases, with and without trajectory reshaping, the inner-loop control reconfiguration and guidance loop adaptation are active. It can be seen that for the case with no reshaping, the vehicle cannot follow the nominal trajectory, and essentially flies straight into the ground. For the case with trajectory reshaping, the vehicle flies a significantly different course. Here, the OPTG algorithm has correctly assigned a commanded trajectory that will not violate the new lift and drag characteristics of the failed vehicle. Figure 11 presents a close-up of the trajectories near touchdown. A smooth main flare to touchdown can be seen for the case with trajectory reshaping.

Figure 12 presents the sink rate history. Here, the touchdown sink rate for the nominal case is approximately  $-2$  fps. For the case with no trajectory reshaping, the touchdown sink rate is approximately  $-25$  fps. This would almost certainly destroy the vehicle. However, the touchdown sink rate for the case with trajectory reshaping is approximately  $-7$  fps, within the acceptable limits of the X-40A. Therefore, even under this very severe failure condition, the vehicle would be able to land without structural damage if it were to possess trajectory-reshaping capabilities.



**Figure 10. Trajectory Profile – Altitude –vs- Downrange.**



**Figure 11. Trajectory Profile Close Up Near Touchdown.**

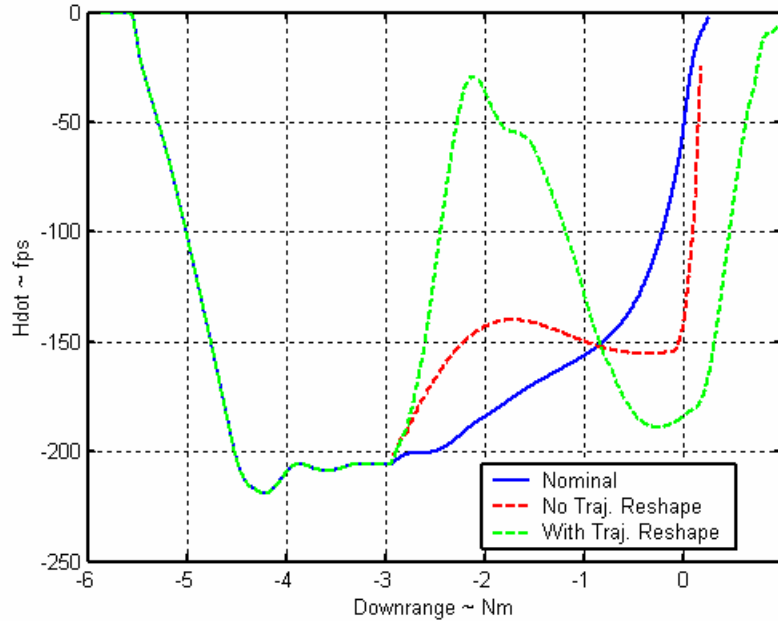


**Figure 12. Sink Rate History.**

Figure 13 presents the flight path angle histories. Here, the nominal flight path at touchdown is approximately  $-1$  deg. For the case with no trajectory reshaping, the touchdown flight path angle is approximately  $-5$  deg., and the touchdown flight path angle for the case with trajectory reshaping is approximately  $-2$  deg. Figure 14 presents the angle-of-attack histories. Here, the nominal angle-of-attack at touchdown is approximately  $12$  deg. For the case with no trajectory reshaping, the touchdown angle-of-attack is significantly high (near the valid limits) at approximately  $24$  deg., whereas the touchdown angle-of-attack for the case with trajectory reshaping is approximately  $15$  deg., well within acceptable values. Lastly, Figure 15 presents the true airspeed history. It can be seen that the touchdown velocity for the case with trajectory reshaping is near that of the nominal case, whereas for the case with no trajectory reshaping, the touchdown velocity is significantly higher.

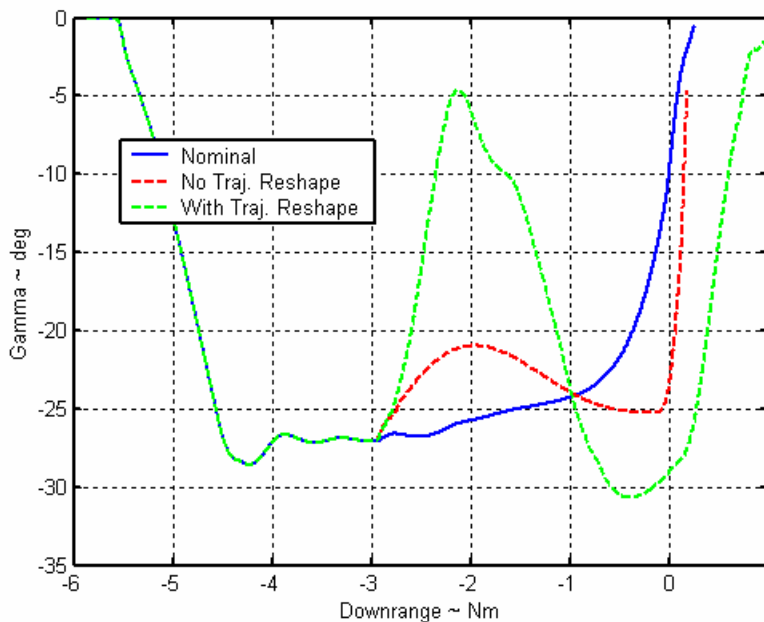


**Figure 13. Flight Path Angle History.**

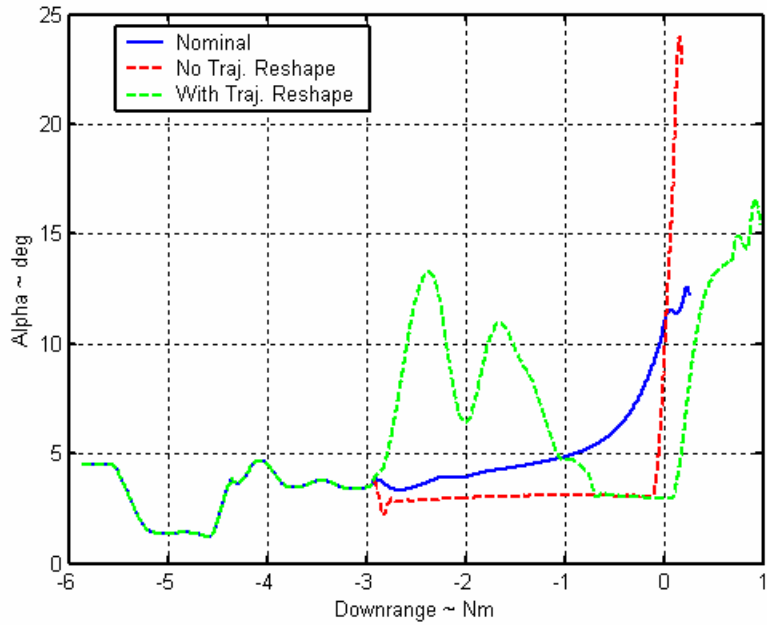


**Figure 14. Angle-of-Attack History.**

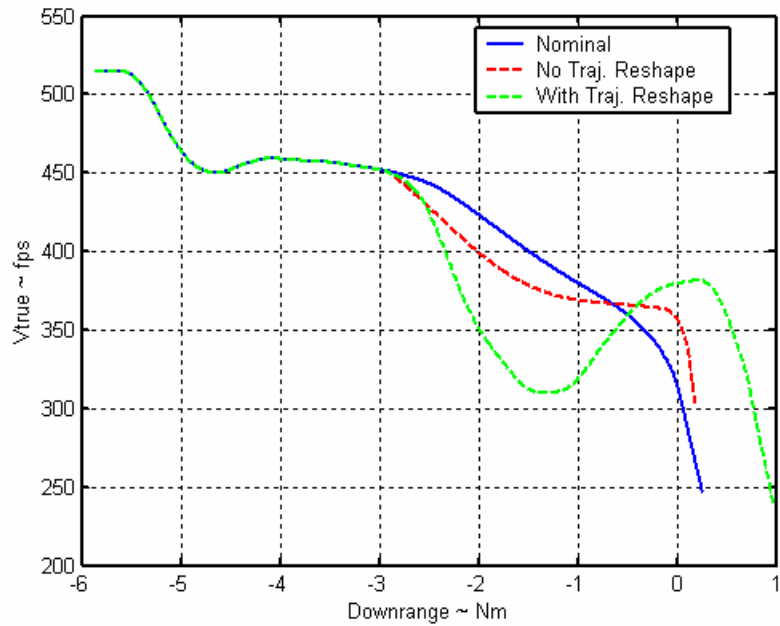


**Figure 15. True Airspeed History.**

## Flight Test Results

The IAG&C flight test program took place over the course of several months in 2003. The GDAIS facilities are located at the Buffalo-Niagara International Airport, and the actual flight tests were conducted at the nearby Niagara Falls Airport, where air traffic is typically at a minimum. Further, this airport possesses an approximately 10,000 foot runway, ideal for such testing. The flight test program was conducted in three main phases, as described below:

1. Calibration Flight Tests: The main purpose of these flight tests was to determine the TIFS research aircraft's ability to simulate X-40A approach/landings. The calibration tests took place during the summer of 2003. Although the TIFS was previously used to simulate Space Shuttle approach and landings, it would now be flown to its structural and aerodynamic limits due to the exceptionally steep glideslopes of typical X-40A RLV approaches (flight path angles of approximately -30 deg.), and its particularly low L/D ratio ( $< 2$ ). The side-force surfaces located on the wings of the TIFS (see Figure 2) are normally used to simulate side forces experienced in flight. However, their main purpose in this program was to generate large amounts of added drag to reduce the L/D ratio of the TIFS. These surfaces were towed out to a constant bias angle during the experiments to a point just before severe buffeting would occur (determined during the calibration tests). It was further established that the TIFS would be unable to sustain steady state flight at the steep glideslopes that would be flown by the X-40A on final approach. To solve this problem, the altitude and sink rate parameters passed to the TIFS model-following algorithms during flight were scaled by a factor of 0.3. In this manner, the TIFS vertical profile was 30% of the X-40A from the start of the trajectory to touchdown. For example, if the X-40A began the approach at 10,000 ft altitude (above ground), then the TIFS would start at 3,000 ft altitude. Their altitudes would only match at touchdown. The advantage of this methodology was that it allowed the TIFS to be used to flight test the IAG&C system. However, the disadvantage was that sensor errors and vertical winds were magnified by the (inverse) scaling process. The altitude and sink rate parameters fed back from the TIFS to the X-40A model included sensor errors and vertical winds, and these parameters were scaled by a factor of 3.3 ( $= 1/0.3$ ). This typically led to larger touchdown sink rates in flight tests than what was observed in batch simulations.
2. Phase I Evaluation Flight Tests: This set of tests occurred September through October, 2003. The main purpose of these tests was to finalize the integrated reconfigurable control and guidance designs, as well as the TIFS model-following protocol. At the end of this phase of the program, the final system designs were completed.
3. Phase II Evaluation Flight Tests: This set of tests occurred November through December, 2003. The final design of the IAG&C system was flight tested during this phase of the program. Here, two "baseline" tests were completed in which the trajectory reshaping was *disabled*. Batch simulations indicated that the vehicle would suffer severe damage, therefore the TIFS needed to land "at altitude" for these baseline runs. For consistency in results, all Phase II tests simulated touchdowns at an altitude of 200 ft. Over 47 calibration and evaluation flight test runs were conducted in six separate flights. The results from this phase of the program are given next.

### A. Phase II Flight Test Results

Typically, one or two nominal runs were first completed for each flight for calibration purposes. In addition to these, there were 40 completed evaluation runs testing 21 different failure combinations. Table 4 presents a summary of the touchdown results for the Phase II evaluation experiments. The runs are listed in chronological order, listing the surfaces failed and the deflection angle of the failures (e.g. L\_Flap(-16), SB(55) = Left flaperon failed at -16 deg. (trailing edge up), Speedbrake locked at 55 deg. (up); also note, R/L\_Rud implies both right and left ruddervators failed). These failure combinations were chosen for their extreme trajectory reshaping characteristics, determined from prior batch simulations experiments. This table lists the touchdown sink rate and pitch attitude for each run. The touchdown specifications on velocity and downrange position were always met, and are therefore not listed. Highlighted are those runs considered to have resulted in successful touchdowns. Although not all of these met the touchdown specifications, they were close enough to be considered successful in light of the

model-following scaling issue on altitude and sink rate, discussed above. This determination was also based on examination of all the state and control histories for these runs.

**Table 4. Summary of Phase II Flight Test Touchdown Results.**

<i>Surfaces Failed</i>	<i>Touchdown</i>		<i>Surfaces Failed</i>	<i>Touchdown</i>	
	<i>Sink Rate</i> ( <i>fps</i> )	<i>Pitch Attitude</i> ( <i>deg.</i> )		<i>Sink Rate</i> ( <i>fps</i> )	<i>Pitch Attitude</i> ( <i>deg.</i> )
L_Flap(-16), SB(55)	-13.4	12.4	R/L_Rud(-2), SB(70)	-19.2	11.8
L_Flap(-16), SB(55)*	-17.0	20.1	R/L_Rud(-2), SB(60)	-10.5	9.1
L_Rud(-4), SB(70)	-7.2	13.7	R/L_Rud(-4), SB(60)	-26.2	16.0
L_Rud(-4), SB(70)*	-21.9	11.5	R/L_Rud(1), SB(60)	+2.0	15.8
SB(70), BF(-20)	-6.8	11.7	R/L_Rud(1), SB(70)	-5.1	13.4
L_Flap(-16), SB(55)	-20.7	14.8	SB(50), BF(20)	-21.3	15.0
L_Rud(-4), SB(60)	-6.6	17.3	R/L_Rud(2), SB(70)	-18.4	12.4
SB(60), BF(-20)	-7.4	12.3	L_Flap(20), SB(60)	-39.2	14.0
R/L_Rud (-4), SB(70)	-8.8	12.2	SB(70), BF(20)	-13.4	18.1
L_Flap(-16), SB(55)	-9.8	17.8	L_Flap(-16), SB(55)	-10.4	16.0
SB(50), BF(20)	-17.4	14.1	R/L_Rud(-4), SB(70)	-15.8	14.6
R/L_Rud (2), SB(70)	-26.0	16.3	R/L_Rud(-4), SB(50)	-12.5	13.8
L_Flap(20), SB(60)	-28.3	14.9	R/L_Rud(-4), SB(60)	-10.0	15.8
L_Rud(-4), SB(50)	-6.6	13.8	R/L_Rud(1), SB(60)	-23.6	19.9
L_Flap(-16), SB(50)	-4.5	13.6	R/L_Rud(-2), SB(60)	-11.8	13.5
L_Flap(20), SB(65)	-2.7	12.3	R/L_Rud(-2), SB(70)	-10.5	17.3
L_Flap(20), SB(70)	-23.0	13.3	L_Flap(20), SB(70)	-7.2	16.0
R/L_Rud(-4), SB(50)	-8.1	11.3	L_Flap(20), SB(60)	-19.0	23.1
R/L_Rud(2), SB(60)	-16.6	19.5	L_Rud(-4), SB(70)	-6.3	14.8
R/L_Rud(-2), SB(70)	-19.2	11.8	SB(70), BF(-20)	-12.2	11.3
SB(50), BF(-20)	-22.6	15.3	SB(60), BF(-20)	-4.7	13.1

\* Trajectory reshaping *disabled*.

There were two main reasons for the unsuccessful runs. First, the Phase II flight tests were plagued with poor weather conditions. Severe winds and turbulence were often encountered, with conditions typically outside original X-40A specifications on acceptable wind conditions. This too was exacerbated by the model-following scaling issue. Secondly, some trajectory reshaping cases were so severe that the TIFS' direct lift flaps saturated during the main flare and the model following results were no longer valid.

Overall, however, the flight tests were quite successful, and under calm winds, several runs indicated consistent results with the batch simulation experiments, validating the IAG&C designs. Lastly, note the two baseline runs (trajectory reshaping disabled) are denoted with a "\*" in the 2<sup>nd</sup> and 4<sup>th</sup> table entries. Comparing these with their counterpart runs in which trajectory reshaping is enabled (the 1<sup>st</sup> and 3<sup>rd</sup> table entries), it can be seen that trajectory reshaping improved the touchdown conditions.

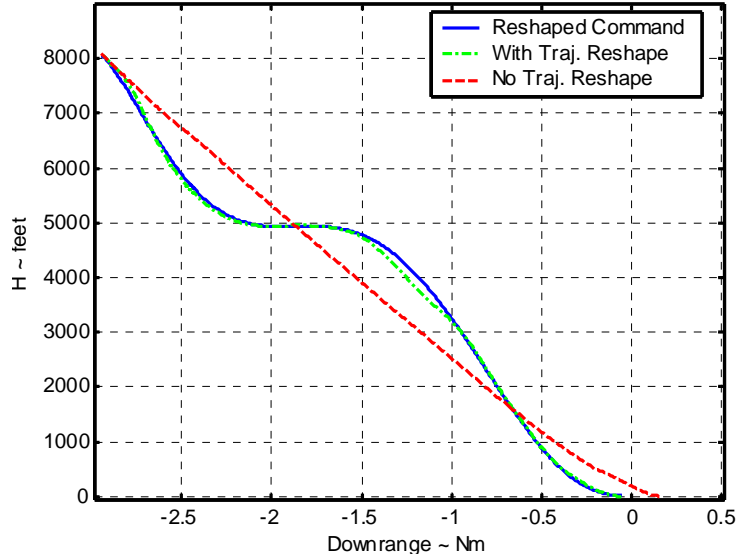
## B. Example Flight Test Results

Results for one flight test experiment are presented below. This experiment was particularly important as it was one of only two experiments where the failure was flown both with and without trajectory reshaping enabled. Further, this failure required the most substantial amount of reshaping in order to recover (changes from the nominal commanded trajectory). The failure was:

Left flaperon failed at -16 deg. (trailing edge up)  
Speedbrake failed at +55 deg. (up)

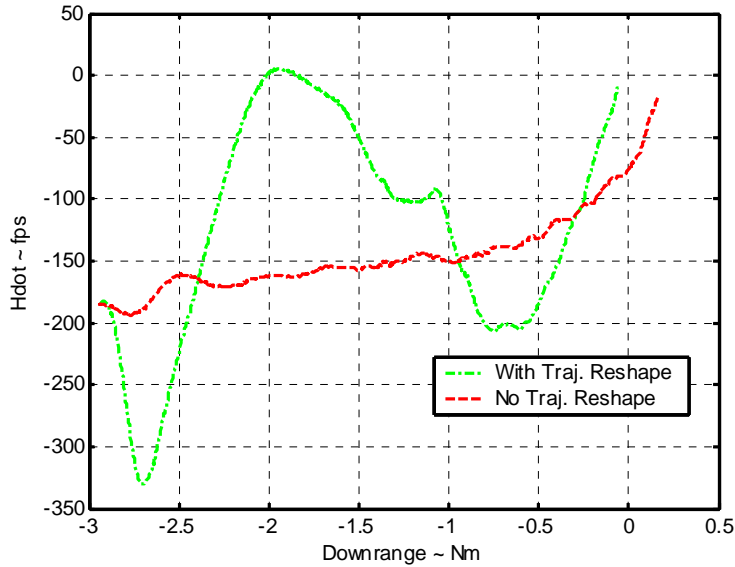
The failure occurs at approximately 3 nautical miles down range from the runway.

Figure 16 presents the trajectory profile (altitude –vs- downrange). Plotted are the reshaped commanded trajectory in the blue solid line (obtained from the OPTG algorithm during flight), the trajectory for the vehicle that follows the reshaped commands in the green dashed line, and the trajectory for the vehicle with no on-line trajectory reshaping in the red dashed line. Note that for both cases, with and without trajectory reshaping, the inner-loop control reconfiguration and guidance loop adaptation are active. For the case with no reshaping, the vehicle cannot follow the nominal trajectory through the main flare, and subsequently hits the ground hard. Obviously for safety reasons, this experiment was performed with the simulated altitude runway defined at 200 ft above the ground. For the case with trajectory reshaping, again, the OPTG algorithm correctly assigns a commanded trajectory that will not violate the new lift and drag characteristics of the failed vehicle. This results in a trajectory whereby the main objective is to preserve the vehicle's energy, given the substantial increase in drag due to both the flaperon and the speedbrake stuck at such a large deflections. It can be seen that the vehicle first dives at a glideslope steeper than nominal. This is done so that it has enough energy to then level off and fly a horizontal path for approximately 0.5 nautical miles. This extends the vehicle's range so that a legitimate touchdown point can be reached in the face of the increased drag. The second steep glideslope allows the vehicle to maintain enough velocity so that a smooth main flare can be executed (the higher the velocity, the more effective the remaining aerodynamic control surfaces become).



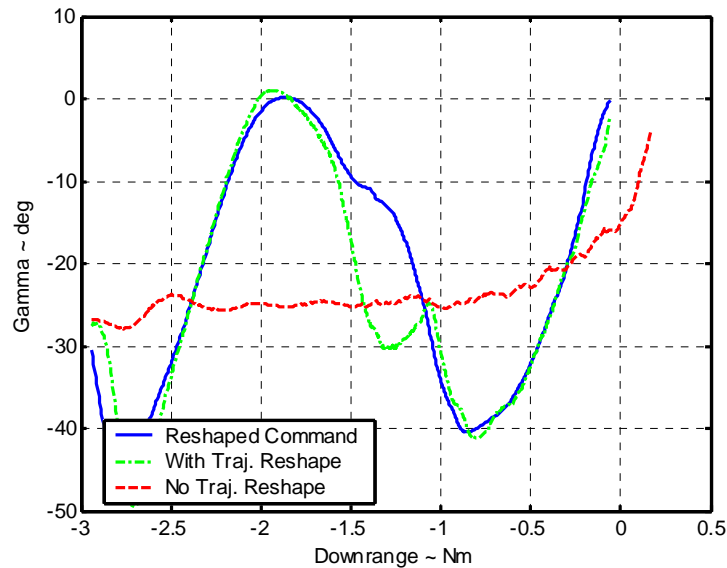
**Figure 16. Flight Test Results: Trajectory Profile – Altitude –vs- Downrange.**

Figure 17 presents the sink rate history. For the case with no trajectory reshaping, the touchdown sink rate is approximately  $-17$  fps. If not destroying the vehicle outright, this would undoubtedly cause major structural damage. However, the touchdown sink rate for the case with trajectory reshaping is approximately  $-9.8$  fps, within the acceptable limits of the X-40A.



**Figure 17. Flight Test Results: Sink Rate History.**

Figure 18 presents the flight path angle histories. Here, the commanded flight path at touchdown targets approximately 0 deg. For the case with no trajectory reshaping, the touchdown flight path angle is approximately  $-4$  deg., and the touchdown flight path angle for the case with trajectory reshaping is approximately  $-2$  deg. Figure 19 presents the angle-of-attack histories. Here, it can be seen that the reshaped commanded angle-of-attack is higher sooner before the main flare, allowing the lift to build up for the main flare. For the case with no trajectory reshaping, the touchdown angle-of-attack is lower before the main flare than it should be, resulting in the significantly high (near the valid limits) angle-of-attack at the end of the trajectory as the vehicle rapidly pulls up in an attempt to follow the commanded flare (however it cannot). Lastly, Figure 20 presents the true airspeed history. Again, the higher velocities at the end of the flight for the reshaped trajectory give the vehicle more control power to execute the main flare, as well as arrest the sink rate just before touchdown. Note, however, that the reshaped commanded velocity is still within acceptable limits to avoid tire blowout.



**Figure 18. Flight Test Results: Flight Path Angle History.**

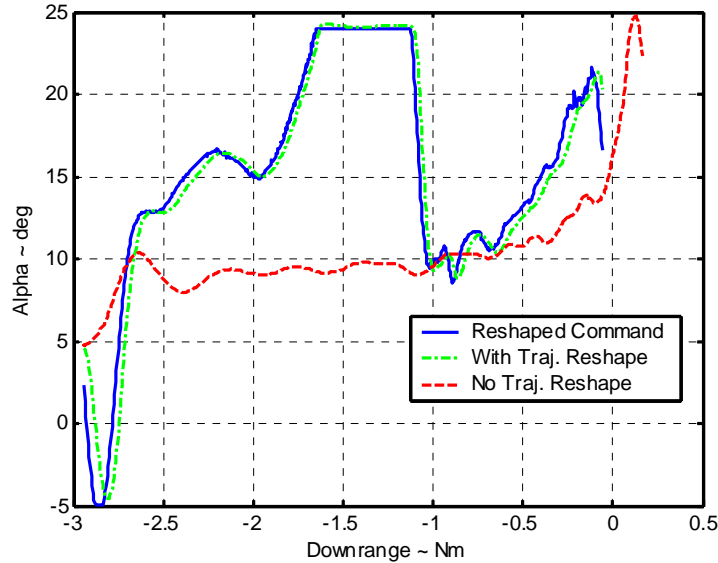


**Figure 19. Flight Test Results: Angle-of-Attack History.**

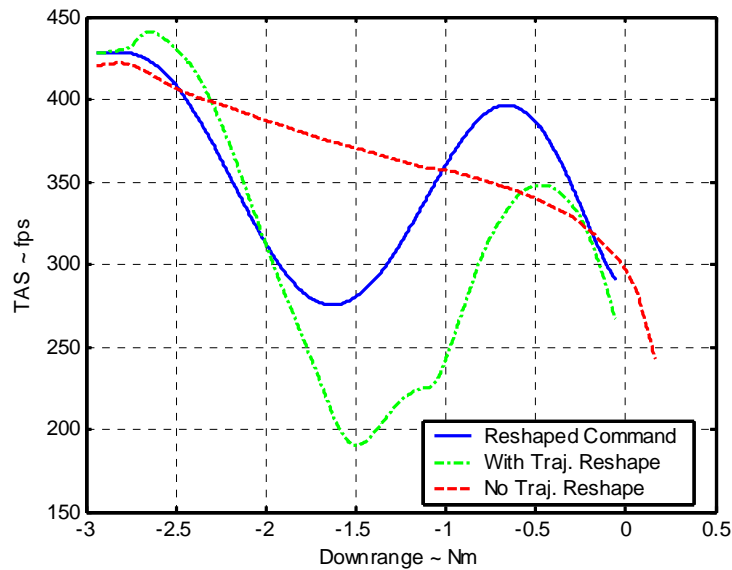


**Figure 20. Flight Test Results: True Airspeed History.**

## VI. Conclusions

Next generation launch technologies will include vehicles with the capacity to reconfigure the control and guidance systems on line, in real time. In conjunction with these functions, the efforts presented in this paper have been to advance the on-line trajectory command reshaping capabilities. It has been shown that for a variety of control effector failures, even with reconfigurable control and guidance systems, trajectory command reshaping is often necessary to recover the mission and achieve acceptable end conditions, such as touchdown sink rate and pitch attitude.

The focus of the paper was to present an adaptive backstepping guidance system that worked in an integrated manner with an autonomous trajectory-reshaping algorithm and a reconfigurable controller. Extensive failure analyses and simulation experiments were performed using a modified version of Boeing's X-40A RLV. The algorithms were then *flight tested* using the Total In-Flight Simulator (TIFS) research aircraft, simulating the X-40A

dynamics. The failure experiments were limited to the approach-to-landing flight phase. Simulation and flight test results were presented, and the results show that some failure cases will require not only control reconfiguration, but guidance adaptation and trajectory reshaping as well in order to recover the mission. Good touchdown conditions were achieved in the face of very severe control effector failures using this new, advanced adaptable/reconfigurable system.

The flight test effort has resulted in a significant maturation of the guidance and trajectory reshaping technologies, and further developments of these approaches continue in related efforts. More advanced hardware-in-the-loop testing is planned for the near future.

### Acknowledgements

This work was funded under two SBIR programs sponsored by (1) the Air Force Research Laboratory, Dr. David Doman, Technical Monitor, and (2) the Marshall Space Flight Center, Mr. Greg Dukeman and Dr. John Hanson, Technical Monitors. *Their support is gratefully appreciated.* Acknowledgments are also due to Boeing, Huntington Beach, which aided in the development and flight testing of the demonstration model, and to General Dynamics Advanced Information Systems (formally Veridian) for their help and advice in the course of the flight test program.

### References

1. Hanson, J. M., "Advanced Guidance and Control Project for Reusable Launch Vehicles," AIAA-2000-3957, Proc. AIAA Guidance, Navigation, and Control Conf., Denver, CO, August, 2000.
2. Hanson, J., "New Guidance for New Launchers," Aerospace America, March, 2003, pp. 36-41.
3. Sharma, M., "Flight-Path Angle Control via Neuro-Adaptive Backstepping," AIAA-2002-4451, Proc. AIAA Guidance, Navigation, and Control Conf., Monterey, CA, Aug. 2002.
4. Schierman, J., Ward, D., Monaco, J., Hull, J., "A Reconfigurable Guidance Approach for Reusable Launch Vehicles," AIAA-2001-4429, Proc. AIAA Guidance, Navigation, and Control Conf., Montreal, Canada, August, 2001.
5. Schierman, J., Hull, J., Ward, D., "Adaptive Guidance with Trajectory Reshaping for Reusable Launch Vehicles," AIAA-2002-4458, Proc. AIAA Guidance, Navigation, and Control Conf., Monterey, CA, Aug. 2002.
6. Schierman, J., Hull, J., Ward, D., "On-Line Trajectory Command Reshaping for Reusable Launch Vehicles," AIAA-2003-5439, Proc. AIAA Guidance, Navigation, and Control Conf., Austin, TX, Aug. 2003.
7. Schierman, J.D., Ward, D.G., Hull, J.R., Gandhi, N., Oppenheimer, M.W., Doman, D.B., "An Approach to Integrated Adaptive Guidance and Control with Flight Test Results," accepted for publication in the *Journal of Guidance, Control, and Dynamics*, approx. 2004.
8. Oppenheimer, M., Doman, D., "Reconfigurable Inner Loop Control of a Space Maneuvering Vehicle," AIAA-2003-5358, Proc. AIAA Guidance, Navigation, and Control Conf., Austin, TX, Aug. 2003.
9. Powell, M., "Variable Metric Methods for Constrained Optimization," *Mathematical Programming: The State of the Art*, (A. Bachem, M. Grotchel and B. Korte, eds.) Springer Verlag, 1983, pp. 288-311.